

# Deep-water dissolved iron cycling and reservoir size across the Ediacaran-Cambrian transition

Lei Xiang<sup>a,\*</sup>, Shane D. Schoepfer<sup>b</sup>, Hua Zhang<sup>a</sup>, Zhen-wu Chen<sup>c</sup>, Chang-qun Cao<sup>a</sup>,  
Shu-zhong Shen<sup>d</sup>

<sup>a</sup> State Key Laboratory of Palaeobiology and Stratigraphy, Nanjing Institute of Geology and Palaeontology and Center for Excellence in Life and Palaeoenvironment, Chinese Academy of Sciences, 39 East Beijing Road, Nanjing 210008, China

<sup>b</sup> Department of Geosciences and Natural Resources, Western Carolina University, 1 University Way, Cullowhee, NC 28779, USA

<sup>c</sup> CAS Key Laboratory of Crust-Mantle Materials and Environment, University of Science and Technology of China, Hefei, Anhui 230026, China

<sup>d</sup> School of Earth sciences and Engineering, Nanjing University, 163 Xianlin Avenue, Nanjing 210023, China

## ARTICLE INFO

Editor: Balz Kamber

### Keywords:

Hetang Formation  
Iron isotope  
Oceanic dissolved iron reservoir  
Oceanic iron cycle  
Cambrian explosion

## ABSTRACT

The majority of the deep ocean was likely under ferruginous conditions during the first four billion years of Earth's history. As the atmosphere was gradually oxygenated, the sources, sinks, redox cycling, and reservoir size of dissolved iron in the deep ocean are likely to have changed dramatically. Whether deep water was thoroughly oxygenated by the time of the Ediacaran-Cambrian transition, and the relationship of this oxygenation to the Cambrian explosion, remains debated. To explore the degree of oceanic oxygenation and its effect on Cambrian explosion, we measured the iron isotopic composition ( $\delta^{56}\text{Fe}$ ) of bulk rock (i.e., cherts and mudstones/shales) through the Piyuncun and Hetang formations, using samples collected from the Chunye-1 core, on the Lower Yangtze Block in western Zhejiang. The limited variation in  $\delta^{56}\text{Fe}$  values ( $< 0.7\text{‰}$ ) and low  $\text{Fe}_T/\text{Al}$  ratios ( $< 0.77$ ) in euxinic samples show that the deep-water  $\text{Fe}^{2+}$  reservoir was quite limited, and likely similar to that of the modern ocean, during the latest Ediacaran and Cambrian Stages 1–3. Iron isotope results, combined with published data from sections on the Middle and Upper Yangtze Block, record a general decline in seawater  $\delta^{56}\text{Fe}$  values from  $> 0.55\text{‰}$  during the end-Ediacaran and Cambrian Stages 1–3 to  $< 0\text{‰}$  during Cambrian Stage 4. Seawater  $\delta^{56}\text{Fe}$  values in the lower and middle Hetang Formation range between 0 and 0.2‰, suggesting that the riverine dissolved and suspended flux and/or aeolian dust was the predominant source of highly reactive iron to the deep basin. Positive deep-water  $\delta^{56}\text{Fe}$  values, above 0.55‰ during the terminal Ediacaran and Cambrian Stages 1–3, likely reflect a basin where pyritization, rather than oxidation, was the predominant sink for deep-water ferrous Fe. Thus, we infer that only the shallow water was sufficiently oxygenated to support complex metazoans and the evolutions of skeletons, and that atmospheric oxygen levels were not high enough to directly oxygenate deep water environments during the Cambrian explosion.

## 1. Introduction

The process of oxygenating Earth's atmosphere, starting from  $< 10^{-5}$  of the present partial pressure of atmospheric oxygen ( $p\text{O}_2$ ) in the Hadean, to levels approximating its present concentration in the early Paleozoic, lasted for  $> 4$  billion years (Lyons et al., 2014). Two great oxidation events (first in the Paleoproterozoic about 2.4 billion years ago, and second in the later Neoproterozoic Era) elevated  $p\text{O}_2$  to  $> 5\%$  of the present atmospheric level (PAL, Canfield and Teske, 1996). After the Neoproterozoic Oxygenation Event (NOE), the surface ocean would have become oxygenated as a result of exchange and equilibration with the atmosphere. Oxygenation of the deep ocean, below the surface

mixed layer, would have presented the greatest obstacle to the establishment of a modern marine redox structure with relatively modern biogeochemical cycles (Lyons et al., 2014). Oxygenic photosynthesis, coupled with burial of organic matter, is the most important source of free oxygen on Earth's surface, and was well established by the Paleoproterozoic (Mills et al., 2014). However, the release of gases and metals in reduced forms from hydrothermal fluids and volcanism would have served as a strong buffer against the accumulation of free oxygen in the deep ocean. Oceanic dissolved ferrous iron ( $\text{Fe}^{2+}$ ), which may have reached concentrations as high as 40 to 120  $\mu\text{M}$  before the advent of oxygenic photosynthesis (Canfield, 2005), may have been the most important reduced metal ion buffering deep water  $\text{O}_2$  accumulation.

\* Corresponding author.

E-mail address: [leixiang@nigpas.ac.cn](mailto:leixiang@nigpas.ac.cn) (L. Xiang).

<https://doi.org/10.1016/j.chemgeo.2020.119575>

Received 13 June 2019; Received in revised form 27 February 2020; Accepted 4 March 2020

Available online 05 March 2020

0009-2541/ © 2020 Elsevier B.V. All rights reserved.

Although iron speciation data suggest that the deep water was pervasively ferruginous from the Archaean through Cambrian Stage 4 (Canfield et al., 2008; Planavsky et al., 2011; Poulton and Canfield, 2011; Sperling et al., 2015; Xiang et al., 2017), the reservoir size and cycling behavior of oceanic  $\text{Fe}^{2+}$  may have evolved dramatically over this period, as the oxygenation of the atmosphere altered the sources and sinks of dissolved iron.

While the astonishing expansion of animal diversity known as the Cambrian explosion was rooted in the Ediacaran, it did not reach its peak until Stage 3 of Cambrian Series 2 (Erwin et al., 2011; Zhu et al., 2017). Whether there was a major deep water oxygenation event prior to or during this metazoan diversification, and whether the diversification can be partially attributed to increasing oxygenation, remains controversial, even among studies employing the same iron speciation geochemical proxies (Li et al., 2017; Sperling et al., 2015). Fe isotope studies, combined with iron elemental geochemical analysis, may offer more comprehensive and mechanistic insight into the deep basin iron cycle, and its implications for the Cambrian explosion.

In this study, we examined the iron isotope composition of bulk rock ( $\delta^{56}\text{Fe}_T$ ) in the basal sediments of the Lower Yangtze Block, using samples collected from the Chunye-1 core. This core is characterized by a continuous sedimentary succession punctuated by recurring euxinic intervals from the Late Ediacaran through Cambrian Stage 4 (Xiang et al., 2017). Previous studies have suggested that the western Zhejiang area was a gulf (termed the Qiantang Gulf, Fig. 1), which was bounded by the Jiangnan Oldland along its western margin and the Cathaysian Oldland along its southeastern margin (Xiang et al., 2017). We used iron isotopes, in combination with iron speciation, to explore the temporal evolution of deep-ocean dissolved iron reservoir size, seawater iron isotopic composition, and the marine iron cycle around the Ediacaran-Cambrian transition, with the aim of better understanding the relationship between atmospheric and oceanic oxygenation and the Cambrian explosion.

## 2. Geologic setting

The Chunye-1 core is located near the village of Hengyan, in Chun'an County, Zhejiang Province, China ( $118^\circ 35' 29.72''\text{E}$ ,  $29^\circ 25' 19.44''\text{N}$ , Fig. 1). The recovered core consists of the Lantian, Piyuncun, Hetang, Dachenling and Yangliugang formations, in ascending order. Lithostratigraphic and chemostratigraphic correlations suggests that the Piyuncun Formation, in the Chunye-1 core represents

a relatively long interval of time, ranging from the Late Ediacaran through Cambrian Stages 1–3. The basal Hetang Formation, in the Chunye-1 core dates to the late Qiongzhusian (late Cambrian Stage 3) at the earliest, and the upper Hetang Formation, very likely represents the Canglangpuian stage (Cambrian Stage 4). Detailed descriptions of the stratigraphy, sedimentology, and biostratigraphic and chemostratigraphic correlations can be found in Xiang et al. (2017).

## 3. Sampling and methods

A total of 40 samples were broken into small pieces (diameter  $\sim 2$  mm) by hammer. After being carefully rinsed five times with deionized water ( $18.2 \text{ M}\Omega$ ) to remove any potential contamination from ferrous field tools, individual pieces were selected for pulverization, avoiding carbonate and pyrite fracture fills, veins, and nodules. The pieces ( $> 50$  g) were then powdered using a SPEX 8515 Shatterbox with a ceramic insert.

Bulk rock Fe isotopic ratios were measured at the University of Science and Technology of China (USTC). Sample dissolution and purification followed previously published procedures (Huang et al., 2011). Briefly, powder samples containing  $\sim 100 \mu\text{g}$  Fe were digested with a mixture of double-distilled, concentrated HCl, HF, and  $\text{HNO}_3$ . Fe was purified using anion exchange resins (Bio-Rad AG1-X8), with Fe recovery  $> 99.9\%$ . Total procedural Fe blanks were consistently  $< 16$  ng. Purified Fe was analyzed using a MC-ICP-MS (Thermo Neptune Plus) in high-resolution mode, with the instrumental mass bias corrected using standard-sample-standard bracketing. Iron isotope data are reported in standard delta notation in per mil (‰) relative to reference material IRMM-014 (IRMM-institute for Reference Material and Methods). This is defined as:

$$\delta^{56}\text{Fe} = [(\delta^{56}\text{Fe}/^{54}\text{Fe})_{\text{sample}}/(\delta^{56}\text{Fe}/^{54}\text{Fe})_{\text{IRMM-014}} - 1] \times 1000 (\text{‰}) \quad (1)$$

To assess the accuracy and long-term external precision of our analyses, three reference materials BIR-1, BCR-2, and AGV-2 were processed with unknown samples for each batch of column chemistry. The long-term external precision ( $2\sigma$ ) of  $\delta^{56}\text{Fe}$  is better than  $0.05\text{‰}$  (Xia et al., 2017). The measured BIR-1, BCR-2, and AGV-2 standards yield  $\delta^{56}\text{Fe}$  values of  $0.050 \pm 0.025\text{‰}$ ,  $0.078 \pm 0.008\text{‰}$ , and  $0.116 \pm 0.060\text{‰}$ , respectively. All of these values are consistent with published values within uncertainty (Craddock and Dauphas, 2011), suggesting that inter-laboratory biases for Fe isotopes are negligible.

The isotopic value of the highly reactive iron pool ( $\text{Fe}_{\text{HR}}$ ) can be

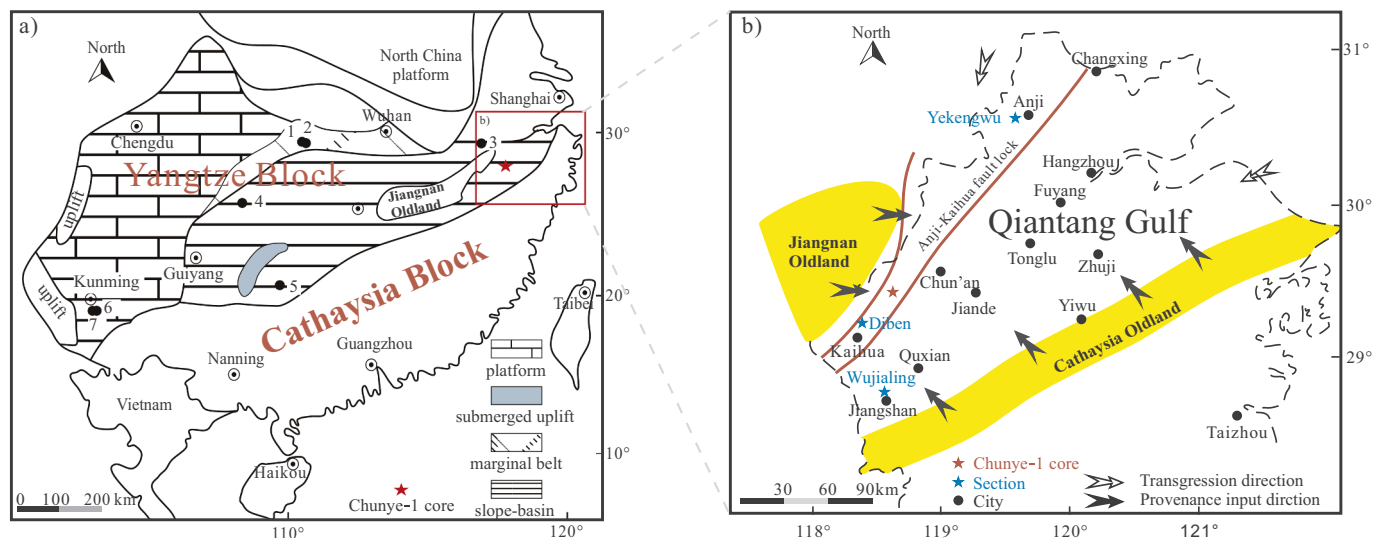


Fig. 1. a) Reconstructed paleogeography of the Yangtze Block during the Late Ediacaran and Cambrian Stage 1; published stratigraphic sections include: 1–Yangjiaping section, 2–Three Gorges drill core, 3–Lantian section, 4–Yinjiang, 5–Silikou, 6–Maotianshan core, 7–Haikou core; b) detailed paleogeographic map of the Qiantang Gulf during the Late Ediacaran to Cambrian Stage 4.

calculated based on the amount of iron in highly reactive forms, and the relatively consistent value of unreactive crustal iron. The speciation of iron in the Chunye-1 samples is reported in Xiang et al. (2017), and those values are used in this study. The isotopic composition of highly reactive iron ( $\delta^{56}\text{Fe}_{\text{HR}}$ ) was then calculated from  $\delta^{56}\text{Fe}_{\text{T}}$  following the formula (Kunzmann et al., 2017):

$$\delta^{56}\text{Fe}_{\text{HR}} = (\delta^{56}\text{Fe}_{\text{T}} - \delta^{56}\text{Fe}_{\text{UR}} \times (1 - \text{Fe}_{\text{HR}}/\text{Fe}_{\text{T}}))/(\text{Fe}_{\text{HR}}/\text{Fe}_{\text{T}}) \quad (2)$$

where  $\delta^{56}\text{Fe}_{\text{UR}}$  is the isotope composition of unreactive crustal iron ( $\sim 0.09\%$ , Beard et al., 2003).

#### 4. Results

Values of  $\delta^{56}\text{Fe}_{\text{T}}$  in the Piyuancun Formation were much higher than those of the Hetang Formation, and also show a greater degree of variability, ranging between 0.08‰ and 0.48‰, with an average value of  $0.24 \pm 0.10\%$  (Fig. 2, Table S1). Measured  $\delta^{56}\text{Fe}_{\text{T}}$  values in the lower and middle Hetang Formation ( $\sim 599.31$  m to 450.1 m) fluctuate between 0.37‰ and  $\sim 0\%$ , with an average value of  $0.14 \pm 0.11\%$  (Fig. 2, Table S1). The uppermost Hetang Formation ( $\sim 445.91$  m to 409.81 m) is characterized by negative  $\delta^{56}\text{Fe}_{\text{T}}$  values, which range from  $-0.14\%$  to 0.11‰, with an average value of  $-0.02 \pm 0.08\%$  (Fig. 2, Table S1).

#### 5. Discussion

##### 5.1. Effects of detrital sheet Fe-silicates

Due to differences in their reaction rates with hydrogen sulfide, iron phases in sediments can be divided into highly reactive iron and unreactive iron pools (Canfield et al., 1992). The iron isotope composition of bulk rock can be viewed as the weighted average of these different mineral phases, i.e.,  $\delta^{56}\text{Fe}_{\text{T}} = \delta^{56}\text{Fe}_{\text{ox}} \times f_{\text{ox}} + \delta^{56}\text{Fe}_{\text{carb}} \times f_{\text{carb}} + \delta^{56}\text{Fe}_{\text{mag}} \times f_{\text{mag}} + \delta^{56}\text{Fe}_{\text{py}} \times f_{\text{py}} + \delta^{56}\text{Fe}_{\text{UR}} \times f_{\text{UR}}$ . Where  $\delta^{56}\text{Fe}_{\text{ox}}$ ,  $\delta^{56}\text{Fe}_{\text{carb}}$ ,  $\delta^{56}\text{Fe}_{\text{mag}}$ ,  $\delta^{56}\text{Fe}_{\text{py}}$  and  $\delta^{56}\text{Fe}_{\text{UR}}$  represent the iron isotope composition of various iron-containing mineral phases, and  $f$  represents their proportional contributions to the total iron pool (Fan et al., 2014; Kunzmann et al., 2017). Substantial part of detrital iron inputs via aeolian dust or riverine water are expected to experience reductive dissolution in anoxic oceanic water masses like that in the Chunye-1 core depositional environment. This soluble iron can then be reprecipitated as highly reactive iron, when dissolved  $\text{Fe}^{2+}$  within the oceanic water column and sedimentary pore waters interacts with free oxygen, hydrogen sulfide, or bicarbonate. This dissolution-reprecipitation process would impart additional iron isotope fractionation effects, with different directions and magnitudes. The rest of insoluble detrital iron in sediments is usually unreactive in the form of sheet silicates (Canfield et al., 1992; Anderson and Raiswell, 2004). The correlation coefficient between Al and  $\text{Fe}_{\text{T}}$ , and between Al and  $\delta^{56}\text{Fe}_{\text{T}}$  is very low ( $R^2 = 0.38$  and 0.02, Fig. 3a, b), indicating Fe in detrital sheet silicates is not a significant contributor to total iron and  $\delta^{56}\text{Fe}_{\text{T}}$ . This is consistent with the fact that  $\text{Fe}_{\text{UR}}$  content in our studied samples was generally lower than 15%, and the difference in  $\delta^{56}\text{Fe}$  between bulk rock and highly reactive iron is small (Fig. 2, Table S1). Thus, the effect of unreactive sheet silicates iron on  $\delta^{56}\text{Fe}_{\text{T}}$  is small, and we can use Formula (1) to effectively correct for it.

##### 5.2. Size of the deep basin $\text{Fe}^{2+}$ reservoir

Values of  $\delta^{56}\text{Fe}_{\text{HR}}$  in the Chunye-1 core range from  $-0.14\%$  to 0.55‰, with an average of 0.16‰ (Fig. 2, Table S1). Variation in  $\delta^{56}\text{Fe}_{\text{HR}}$  values ( $< 0.7\%$ ) is the primary driver of  $\delta^{56}\text{Fe}_{\text{T}}$  values. The range of observed  $\delta^{56}\text{Fe}_{\text{HR}}$  values is much narrower than that observed in banded iron formations (BIFs, Dauphas et al., 2017; Halverson et al., 2011; Rouxel et al., 2005), or in other Neoproterozoic sediments after BIF deposition terminated (Kunzmann et al., 2017; Zhang et al., 2015). We take this to indicate that, although the deep water was generally ferruginous from the Archean through the early Cambrian (Canfield

et al., 2008; Planavsky et al., 2011; Poulton and Canfield, 2011; Sperling et al., 2015), the oceanic dissolved Fe reservoir around the Ediacaran-Cambrian transition may have shrunk dramatically to well below that before ca. 570 Ma (Canfield, 2005; Kunzmann et al., 2017).

While a  $\text{Fe}_{\text{py}}/\text{Fe}_{\text{HR}}$  threshold of  $> 0.80$  is often used to distinguish euxinia from ferruginous conditions, this value is based on modern sediments for which  $\text{Fe}_{\text{mag}}$  and  $\text{Fe}_{\text{carb}}$  were not determined (Poulton and Canfield, 2005), and the 0.70 threshold of Poulton and Canfield (2011) may be more appropriate in this setting (Raiswell et al., 2018). Adopting this new criteria, the Piyuancun and Hetang formations in the Chunye-1 core can be subdivided into two continuous euxinic intervals ( $\sim 594.46$  m to 528.81 m, and  $\sim 466.21$  m to 407.76 m) and another two intervals dominated by ferruginous bottom water with intermittent euxinic conditions ( $\sim 707.21$  m to 596.26 m, and  $\sim 521.61$  m to 468.91 m, Fig. 2, Table S2). Under iron-limited euxinic conditions, we would expect nearly all  $\text{Fe}^{2+}$  to precipitate as sulfides. Thus, when the speciation of highly reactive iron indicates pervasive euxinia, we can use the aluminum-normalized total iron content ( $\text{Fe}_{\text{T}}/\text{Al}$ ) to constrain the size of the marine  $\text{Fe}^{2+}$  reservoir (Anderson and Raiswell, 2004).

Average  $\text{Fe}_{\text{T}}/\text{Al}$  ratios for euxinic samples were 0.58 ( $n = 32$ ) in the Piyuancun Formation, 0.60 ( $n = 26$ ) in the lower Hetang Formation, and 0.59 ( $n = 9$ ) in the Middle Hetang Formation (Fig. 2, Table S2). These values are only slightly elevated above the average crustal ratio (0.48), and few values exceed the threshold indicating some degree of authigenic iron enrichment ( $> 0.77$ ; Cole et al., 2017, Fig. 2, Table S2), indicating that there was no major addition of highly reactive iron above ordinary crustal levels (Raiswell et al., 2018) in the Chunye-1 core depositional environment. This combination of limited variation in  $\delta^{56}\text{Fe}_{\text{HR}}$  values and rather low  $\text{Fe}_{\text{T}}/\text{Al}$  ratios, even in euxinic samples, indicates that the deep-water  $\text{Fe}^{2+}$  reservoir was quite limited during the latest Ediacaran and Cambrian Stages 1–3 (Rouxel et al., 2005). This limited authigenic Fe deposition, as reflected in a relatively low  $\text{Fe}_{\text{T}}/\text{Al}$  ratios, also observed in many euxinic deposits from shallower environments around the Yangtze Block during Cambrian Stages 1–3; these include the Haikou core and Maotianshan core from the Upper Yangtze platform (Hammarlund et al., 2017), the Yangjiaping section on the Middle Yangtze platform (Feng et al., 2014), and the Liantian section on the Lower Yangtze platform (Cheng et al., 2017).

##### 5.3. Seawater $\delta^{56}\text{Fe}$ values

The oxidation of dissolved  $\text{Fe}^{2+}$  into particulate ferric (oxyhydr) oxides or magnetite is associated with Fe isotope fractionation, with the heavier isotope being incorporated into minerals. The largest fractionation factors are  $\sim -2.76$  to  $-2.87\%$  for (oxyhydr)oxide formation and  $-1.6\%$  for magnetite formation (Bullen et al., 2001; Welch et al., 2003; Frierdich et al., 2014; Kunzmann et al., 2017). Iron speciation analyses (Xiang et al., 2017) indicate that iron oxides and magnetite combined make up  $< 10\%$  of highly reactive iron in the Piyuancun Formation (Fig. 2, Table S1). Thus, the fractionation associated with the formation of these minerals should not exert a major control on  $\delta^{56}\text{Fe}_{\text{HR}}$  values. The remainder of the highly reactive iron pool ( $> 90\%$ ) is associated with carbonate and pyrite (Fig. 2, Table S1). The maximum fractionation factor associated with the precipitation of carbonate-associated iron ( $\Delta^{56}\text{Fe}_{\text{Fe-FeCO}_3} = 0.48 \pm 0.22\%$ , Wiesli et al., 2004) is significantly smaller than that associated with pyrite formation ( $\Delta^{56}\text{Fe}_{\text{Fe-pyrite}} = \sim 2.2\%$ , Guilbaud et al., 2011; Rolison et al., 2018), though the direction of  $\delta^{56}\text{Fe}$  fractionation is the same for both reactions.

The chert units of the Piyuancun Formation were mainly deposited under ferruginous conditions, interrupted by intermittent euxinia (Fig. 2). Unlike the more persistently euxinic intervals seen in the lower and upper Hetang Formation (Fig. 2, Table S2), these discontinuous Piyuancun euxinic intervals did not allow total dissolved sulfide ( $\Sigma\text{H}_2\text{S} = \text{S}^{2-} + \text{HS}^- + \text{H}_2\text{S}$ ) to accumulate to high concentrations before encountering  $\text{Fe}^{2+}$ -rich water masses. Sulfide concentrations are

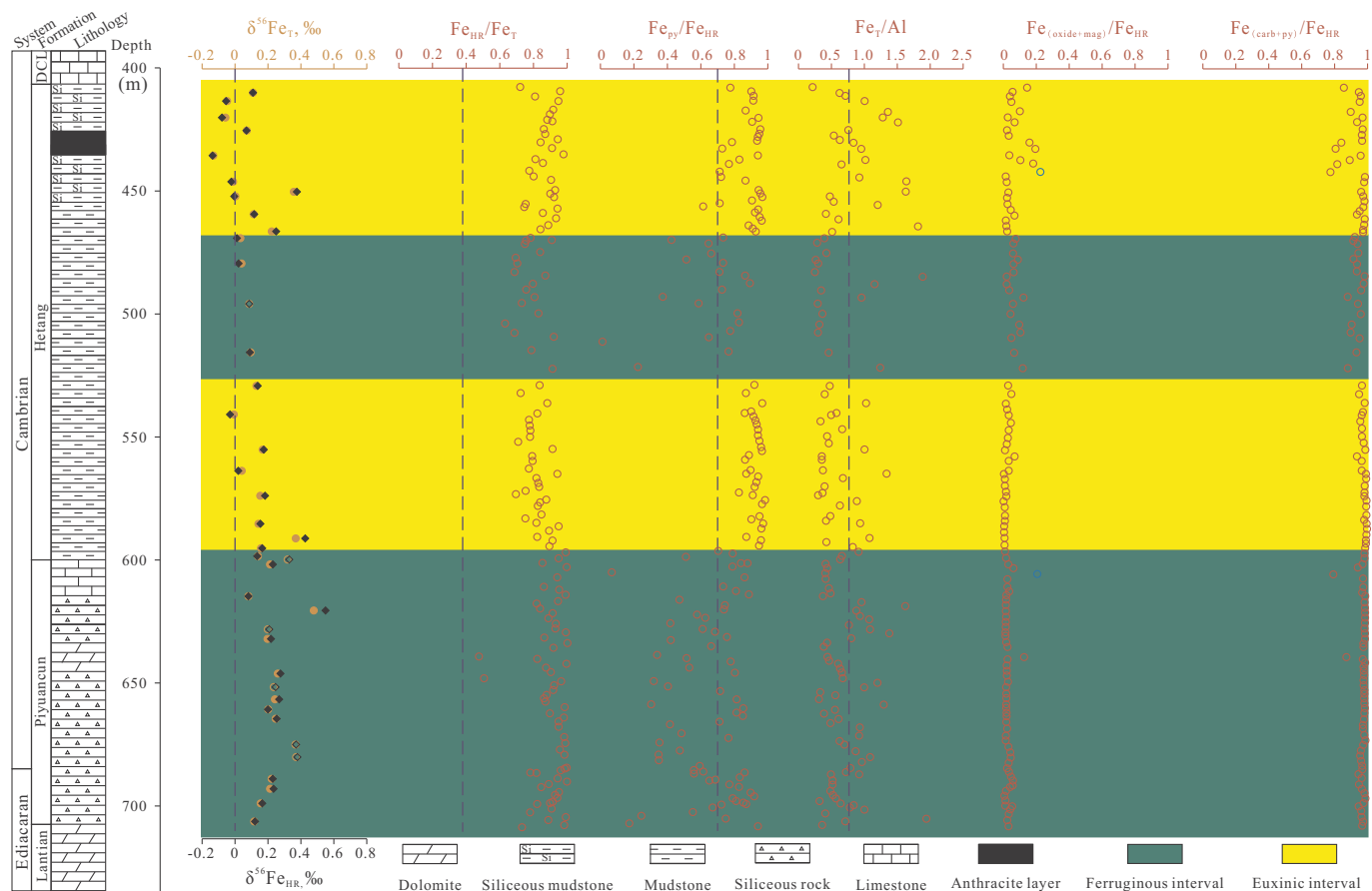


**Fig. 2.** Stratigraphic distribution of the iron isotopic composition of bulk rock ( $\delta^{56}\text{Fe}_T$ ) and the calculated isotopic composition of highly reactive iron ( $\delta^{56}\text{Fe}_{\text{HR}}$ ), as well as ratios of  $\text{Fe}_{\text{HR}}/\text{Fe}_T$ ,  $\text{Fe}_{\text{py}}/\text{Fe}_{\text{HR}}$ ,  $\text{Fe}_T/\text{Al}$ ,  $\text{Fe}_{(\text{carb}+\text{py})}/\text{Fe}_{\text{HR}}$ , and  $\text{Fe}_{(\text{oxide}+\text{mag})}/\text{Fe}_{\text{HR}}$  in the Chunye-1 core (from Xiang et al., 2017). Note that solid circles and diamonds represent samples deposited under euxinic conditions; open circles and diamonds represent sample deposited under ferruginous conditions.  $\text{Fe}_{(\text{carb}+\text{py})}/\text{Fe}_{\text{HR}}$  represents the proportion of the highly reactive iron pool that is associated with carbonate and pyrite.  $\text{Fe}_{(\text{oxide}+\text{mag})}/\text{Fe}_{\text{HR}}$  represents the proportion of the highly reactive iron pool that is associated with oxides and magnetite.

likely to have been relatively low ( $< 50 \mu\text{M}$ ), similar to those seen in the upper euxinic water mass of the modern Black Sea (Rolison et al., 2018, see Fig. 2). The precipitation of dissolved ferrous iron during deposition of the Piyuancun Formation, including during the intermittent euxinic intervals, may not have been quantitative. Thus, this incomplete precipitation of  $\text{Fe}^{2+}$  would impart an iron isotope fractionation between pyrite and the oceanic dissolved ferrous iron pool;  $\delta^{56}\text{Fe}$  values of pyrite in the weakly euxinic interval of the Piyuancun Formation may be lighter than contemporaneous seawater  $\delta^{56}\text{Fe}$  values. Measured  $\delta^{56}\text{Fe}_{\text{HR}}$  values in the Piyuancun Formation range between 0.08‰ and 0.55‰, with an average of  $0.25 \pm 0.11\%$ . We infer that oceanic  $\delta^{56}\text{Fe}$  values would not have been  $< 0.25\%$ , and were most likely  $> 0.55\%$ , during the terminal Ediacaran and Cambrian Stages 1–3.

This inference is corroborated by the high  $\delta^{56}\text{Fe}$  values observed in other marginal belt and, slope-basin sediments from the Middle and Upper Yangtze Block during the Ediacaran-Cambrian transition. The Silikou section shows values as high as to 0.86‰, while the Three Gorges region yields values  $> 1\%$  (Fig. 4, Fan et al., 2018; Sawaki et al., 2018). While we unfortunately lack  $\delta^{56}\text{Fe}$  records from outside of South China, these sections on the Yangtze Block are distributed over a distance of several thousands of kilometers (Fig. 1), and we can reasonably infer that the positive oceanic  $\delta^{56}\text{Fe}$  values are regional or possibly global signals. Mo/TOC ratios in the Chunye-1 core also show a temporal pattern that agrees well with platform, margin, and slope/basin sections from across the South China Block, suggesting the region was in communication with the open ocean (Xiang et al., 2017).

As reactive iron would be quantitatively sequestered in sulfides under strongly euxinic conditions, sedimentary  $\delta^{56}\text{Fe}_{\text{HR}}$  values may be a faithful recorder of seawater  $\delta^{56}\text{Fe}$  values during deposition of the Hetang Formation (Planavsky et al., 2012; Rolison et al., 2018; Rouxel et al., 2005). The average  $\text{Fe}_{\text{py}}/\text{Fe}_{\text{HR}}$  ratios of the lower and upper Hetang Formation were 0.92 and 0.86 respectively, suggesting that these strata were deposited under strongly euxinic conditions (Fig. 2, Table S2). If so, seawater  $\delta^{56}\text{Fe}$  values during deposition of the lowermost Hetang Formation were similar to those during deposition of the Piyuancun Formation, generally  $> 0.55\%$ . During deposition of the Lower Hetang Formation, seawater  $\delta^{56}\text{Fe}$  values apparently dropped to approximately 0.1‰, while during deposition of the uppermost Hetang interval (Cambrian Stage 4), seawater  $\delta^{56}\text{Fe}$  values were  $< 0\%$ . This pattern reflects a general decline in the  $\delta^{56}\text{Fe}$  of dissolved seawater  $\text{Fe}^{2+}$  from the end-Ediacaran through Cambrian Stage 4 (Fig. 2).

#### 5.4. The oceanic $\text{Fe}^{2+}$ cycle: sources and sinks

The isotopic composition of the deep water iron pool is controlled by the relative fluxes of various sources of iron into the ocean, the oceanic iron redox cycle, and diverse fluid-mineral fractionation pathways (Conway and John, 2014; Dauphas et al., 2017; Kunzmann et al., 2017). Aeolian dust, hydrothermal fluids, and reductive dissolution of sedimentary minerals are commonly viewed as the dominant sources of Fe to deep basin environments (Dauphas et al., 2017; Horner et al., 2015). Paleogeographic reconstructions of the Yangtze Block show an uplift, called Jiangnan Oldland, located several tens of kilometers west

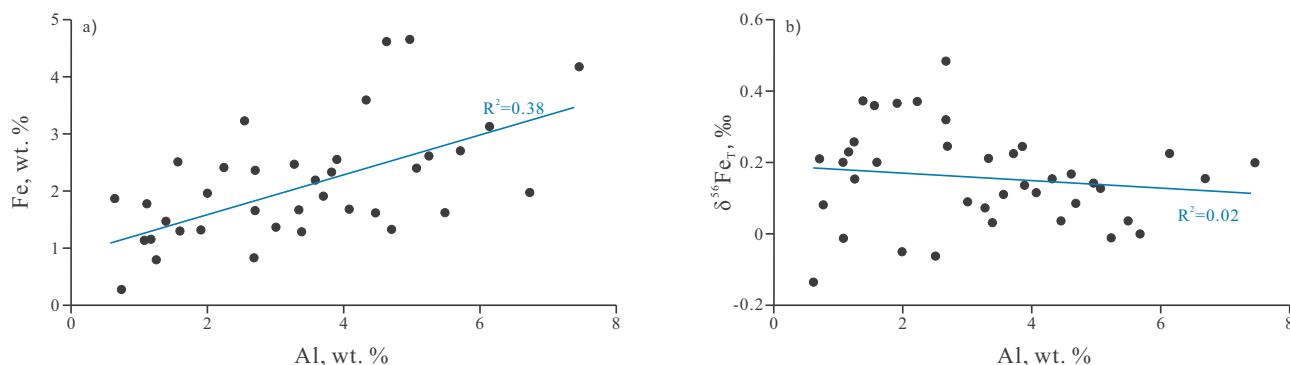


Fig. 3. Crossplots of Al versus  $\text{Fe}_T$  and  $\delta^{56}\text{Fe}_T$  in the Chunye-1 core.

of the Chunye-1 core depositional environment (Fig. 1a). Riverine water draining from this exposed land may have carried fine nanoparticles, colloidal, and aqueous iron into the basin (Raiswell and Canfield, 2012; Scholz et al., 2019). Other sources, such as ice-rafted sediments containing  $\text{Fe}^{2+}$  account for only a small proportion of deep basinal iron input (Raiswell and Canfield, 2012). Due to the pervasively anoxic conditions in deep water environments during the Ediacaran-Cambrian transition (Canfield et al., 2008; Yuan et al., 2014; Cheng et al., 2017; Chang et al., 2018; Fan et al., 2018), the non-reductive dissolution of terrigenous sediments (which can yield dissolved Fe with a  $\delta^{56}\text{Fe}$  values as high  $0.37 \pm 0.15\text{‰}$ ) is not likely to have been a major source of dissolved iron (Radic et al., 2011). The  $\delta^{56}\text{Fe}$  values of most natural aeolian dust within a small range of variation, around  $0.13 \pm 0.18\text{‰}$  (Waeles et al., 2007). The  $\delta^{56}\text{Fe}$  values of hydrothermal fluids are typically much more depleted than those of aeolian dust, ranging from  $-1\text{‰}$  to  $0$  (Bennett et al., 2009; Eroglu et al., 2018). River has a dissolved and suspended  $\delta^{56}\text{Fe}$  composition of  $-1.0\text{‰}$  to  $+0.3\text{‰}$ , but most samples plot in the range of  $-0.1\text{‰}$  to  $+0.3\text{‰}$  (Kiczka et al., 2011; Dauphas et al., 2017; Kunzmann et al., 2017). Of the major dissolved iron inputs, dissimilatory iron reduction (DIR) in organic-rich sediments produces the most depleted  $\delta^{56}\text{Fe}$  values (as low as  $-0.5\text{‰}$  to  $-3.4\text{‰}$ , Duan et al., 2010; Severmann et al., 2008).

The seawater  $\delta^{56}\text{Fe}$  values recorded in the Piyuncun Formation and basal Hetang Formation are higher than any of these four major end-member Fe sources. The total sedimentary iron pool in the Piyuncun and lower-middle Hetang formations is dominated by highly reactive iron, despite showing no evidence for authigenic iron enrichment in the form of elevated  $\text{Fe}_T/\text{Al}$  ratios. This observation suggests that the highly reactive iron in the oceanic water column is derived from microbially mediated conversion of originally unreactive detrital iron phases (Raiswell et al., 2018), and/or from the preferential transport of terrestrial nanoparticles and colloids with a high reactive Fe content by riverine water (Scholz et al., 2019).

One possible explanation is that the reduction of ferric oxides in marine sediments released dissolved  $\text{Fe}^{2+}$  with a relatively low  $\delta^{56}\text{Fe}$  values, resulting in both low  $\text{Fe}_T/\text{Al}$  ratios and enriched  $\delta^{56}\text{Fe}$  values in the residual sediment. While the  $\text{Fe}_T/\text{Al}$  ratios of ferruginous intervals in the middle Hetang Formation are typical lower than those seen in Cambrian sediments from oxic platform environments (0.43 to 0.51, Wen et al., 2015; Hammarlund et al., 2017; Qi et al., 2018), their  $\delta^{56}\text{Fe}_T$  and calculated  $\delta^{56}\text{Fe}_{\text{HR}}$  values fall within the range of crustal values, suggesting they have not been strongly affected by dissimilatory reduction. The weakly positive correlation ( $R^2 = 0.15$ ) between  $\delta^{56}\text{Fe}_{\text{HR}}$  values and  $\text{Fe}_T/\text{Al}$  ratios within the Piyuncun Formation also negates

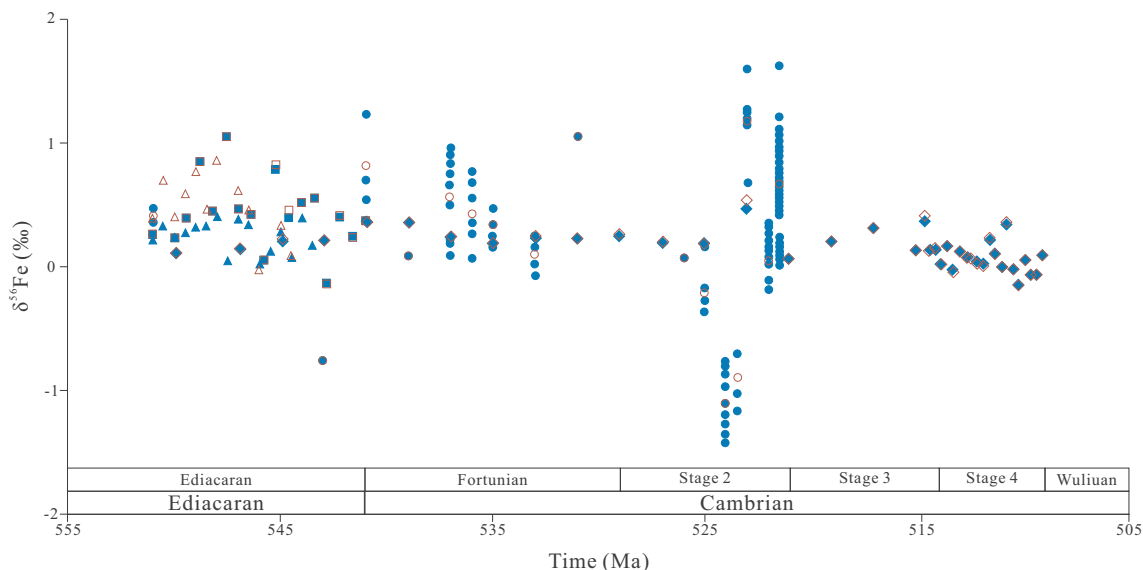


Fig. 4. Summary of  $\delta^{56}\text{Fe}$  results over the terminal Ediacaran and Cambrian Stage 1–4. Solid blue circle represents the  $\delta^{56}\text{Fe}$  value of pyrite grains in the drill cores at three Gorges using laser ablation multi collector inductively coupled plasma mass spectrometry (Sawaki et al., 2018), and Open red circle represents the average  $\delta^{56}\text{Fe}$  value of each pyrite grain at certain depth in the drill cores at three Gorges. Solid blue and open red triangle respectively represent the  $\delta^{56}\text{Fe}_T$  and  $\delta^{56}\text{Fe}_{\text{HR}}$  values of Silikou section (Fan et al., 2018). Solid blue and open red square respectively represent the  $\delta^{56}\text{Fe}_T$  and  $\delta^{56}\text{Fe}_{\text{HR}}$  values of Yinjiang section (Fan et al., 2018). Solid blue and open red diamond respectively represent the  $\delta^{56}\text{Fe}_T$  and  $\delta^{56}\text{Fe}_{\text{HR}}$  values at the Chunye-1 core. (For interpretation of the references to colour in this figure legend, the reader is referred to the web version of this article.)

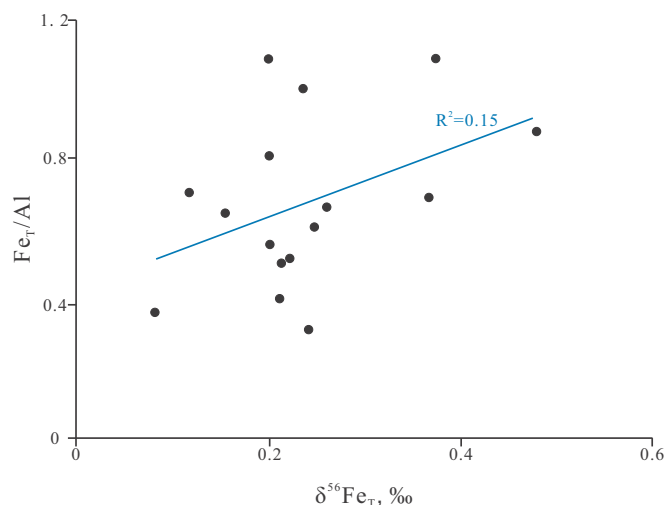


Fig. 5. Crossplot of  $\delta^{56}\text{Fe}_T$  versus  $\text{Fe}_T/\text{Al}$  of Piyuancun Formation in the Chunye-1 core.

this possibility (Fig. 5). No apparent net gain in authigenic iron with low  $\delta^{56}\text{Fe}$  values occurred during the euxinic intervals of Piyuancun deposition, and the net loss of highly reactive iron in the ferruginous intervals did not simultaneously drive an increase in the  $\delta^{56}\text{Fe}$  composition of residual iron. Thus, in situ dissimilatory iron reduction cannot explain the positive  $\delta^{56}\text{Fe}$  values observed in the Piyuancun Formation.

Sulfide and oxygen are the two anions most likely responsible for the removal of  $\text{Fe}^{2+}$  in deep basinal waters (Canfield, 1998). The incorporation of  $\text{Fe}^{2+}$  into sulfides and carbonates preferentially selects for the lighter isotope, enriching the residual dissolved  $\text{Fe}^{2+}$  pool in  $^{56}\text{Fe}$ . In contrast, oxidation of  $\text{Fe}^{2+}$  to form ferric oxides and magnetite results in incorporation of heavy Fe isotopes into the mineral phases, such that the  $\delta^{56}\text{Fe}$  of residual dissolved  $\text{Fe}^{2+}$  becomes increasingly depleted (Bullen et al., 2001; Frierdich et al., 2014). The isotope fractionation factor between ferrous iron and syngenetic pyrite is  $\sim 2.2\%$  (Rolison et al., 2018), and the isotope fractionation factor between ferrous iron and syngenetic ferric species ranges between  $\sim 2.76\%$  and  $\sim 2.87\%$  (Welch et al., 2003). Thus, the precipitation of pyrite or iron oxides would alter the  $\delta^{56}\text{Fe}$  value of the residual dissolved ferrous iron in opposite direction, albeit with similar magnitude. Positive deep-ocean  $\delta^{56}\text{Fe}$  values, above  $0.55\%$ , or even  $> 1\%$  in the Piyuancun and basal Hetang formations, likely reflects the predominance of sulfide precipitation relative to oxide precipitation in a redox stratified ocean during the terminal Ediacaran and Cambrian Stages 1–3 (Dauphas et al., 2017; Horner et al., 2015; Klar et al., 2017; Rouxel et al., 2005). This process would enrich the residual oceanic dissolved  $\text{Fe}^{2+}$  pool, such that during episodes of euxinia on the South China Block, the near quantitative precipitation of sulfides reflects this overall  $\delta^{56}\text{Fe}$  enrichment. This interval of globally intense sulfide precipitation may also be responsible for the coeval decrease in the size of the oceanic Mo and U reservoir (Xiang et al., 2017).

Measured  $\delta^{56}\text{Fe}_{\text{HR}}$  values in the lower and middle Hetang Formation range between 0 and  $0.2\%$ , similar to the values seen in bulk continental crust ( $\sim 0.09\%$ , Beard et al., 2003). It is likely that the predominant  $\text{Fe}^{2+}$  source during this interval was terrigenous, Fe-containing minerals, whether carried by wind or riverine water, from exposed continental landmasses (Raiswell and Canfield, 2012). The combination of low  $\text{Fe}_T/\text{Al}$  ratios ( $\leq 0.6$ ) with high  $\text{Fe}_{\text{HR}}/\text{Fe}_T$  ratios ( $> 0.8$ ) implies that a terrigenous iron flux, from aeolian dust or riverine water, may also have been the dominant iron source during deposition of the Piyuancun and lower-middle Hetang formations. Hydrothermal fluids are generally regarded as the predominant Fe source to the early Precambrian ocean (Planavsky et al., 2012), and preserved

hydrothermal vents have been described from the marginal zone in South China (Chen et al., 2009). However, our iron elemental and isotopic results suggest that the contribution of hydrothermal vent-derived Fe did not increase the oceanic dissolved  $\text{Fe}^{2+}$  reservoir to higher than modern levels (Raiswell et al., 2018).

Measured  $\text{Fe}_T/\text{Al}$  ratios of the Piyuancun and lower-middle Hetang formations in the Chunye-1 core can be compared with published  $\text{Fe}_T/\text{Al}$  ratios from contemporaneous environments on the Yangtze Block. These include platform sections such as the Meishucun section (Wen et al., 2015), the Weng'an section (Jin et al., 2016), Jinsha section (Jin et al., 2016) and the Maotianshan area sections containing the famous Chengjiang biota (Hammarlund et al., 2017; Qi et al., 2018), as well as anoxic transitional zone sections, such as the Yinjiang section (Fan et al., 2018), and the Wangjiaping section (Jin et al., 2017). Other deep basinal sections, such as the Lantian section (Cheng et al., 2017) can also be included in the synopsis. When compiling data from these sections, we found that the average  $\text{Fe}_T/\text{Al}$  ratios in platform environments range from 0.43 and 0.51, within the range of Upper Continental Crust values; average ratios in the transitional zone were approximately equal, between 0.4 and 0.55, and average ratios in the basinal Lantian section ( $\sim 0.6$ ) were only slightly enriched above those seen in oxic platforms or the anoxic transitional zone.

The spatial distribution of  $\text{Fe}_T/\text{Al}$  ratios across South China in Cambrian Stages 1–3 is inconsistent with an ‘iron-shuttling’ model based on the modern Black Sea (Lyons and Severmann, 2006), in which iron dissolved in the anoxic pore water or shelf areas is shuttled into the deeper basin and reprecipitated in reactive forms. The absolute values of  $\text{Fe}_T/\text{Al}$  ratios within the basinal Lantian section and Chunye-1 core are much lower than those seen in the euxinic Black Sea basin ( $\sim 1$ , Lyons and Severmann, 2006). Thus, the low  $\text{Fe}_T/\text{Al}$  ratios and absence of extremely depleted  $\delta^{56}\text{Fe}$  values seen in the Piyuancun and lower-middle Hetang formations of Chunye-1 core indicate that the shelf-to-basin ‘iron shuttle’ was not operating in this time interval (Severmann et al., 2008); basin sediments do not seem to have received any additional iron liberated from shelf sediments by dissimilatory iron reduction. The existence of a ‘euxinic wedge’ at chemocline water depths during the terminal Ediacaran and Cambrian Stages 1–3 may have cut off the lateral transport of mobile ferrous iron from shallow shelf environments to the mainly-ferruginous deep basin (Fig. 6a, Feng et al., 2014).

There is a marked rise in average  $\text{Fe}_T/\text{Al}$  ratios, from  $\sim 0.60$  in the Piyuancun and lower-middle Hetang formations, to 1.97 ( $n = 27$ , Table S2) in the upper Hetang Formation. This strongly indicates that addition of a new, exogenous source of highly reactive iron in addition to the unreactive lithogenous component of  $\text{Fe}_T$ . Enhanced input of hydrothermal  $\text{Fe}^{2+}$  could simultaneously drive the enrichment of highly reactive Fe and the observed decrease in  $\delta^{56}\text{Fe}$  values, but cannot explain the simultaneous enrichment of Mo, U, and Fe in this interval, since the former two metals are generally depleted in hydrothermal fluids (Kendall et al., 2017; Partin et al., 2013). Inferred seawater  $\delta^{56}\text{Fe}$  values in the uppermost Hetang Formation are negative. When combined with the modern-like oceanic Mo and U reservoir during deposition of the uppermost Hetang Formation (Xiang et al., 2017), one possible interpretation is that the oxic surface water-mass had expanded downward from shallow shelf environments and into deeper water. The contraction of the ‘euxinic wedge’ would have allowed for the onset of lateral iron shuttling, promoting both increased  $\text{Fe}_T/\text{Al}$  ratios and decreased  $\delta^{56}\text{Fe}$  values in basinal sediments (Fig. 6b, Severmann et al., 2008).

## 6. Implications

While South China contains an abundant fossil record from the end-Ediacaran through Cambrian Stage 3, nearly all of the reported fossil assemblages represent shallow shelf or mixed-layer water depths, rather than deeper slope-basin facies. Our  $\delta^{56}\text{Fe}$  results from the Piyuancun

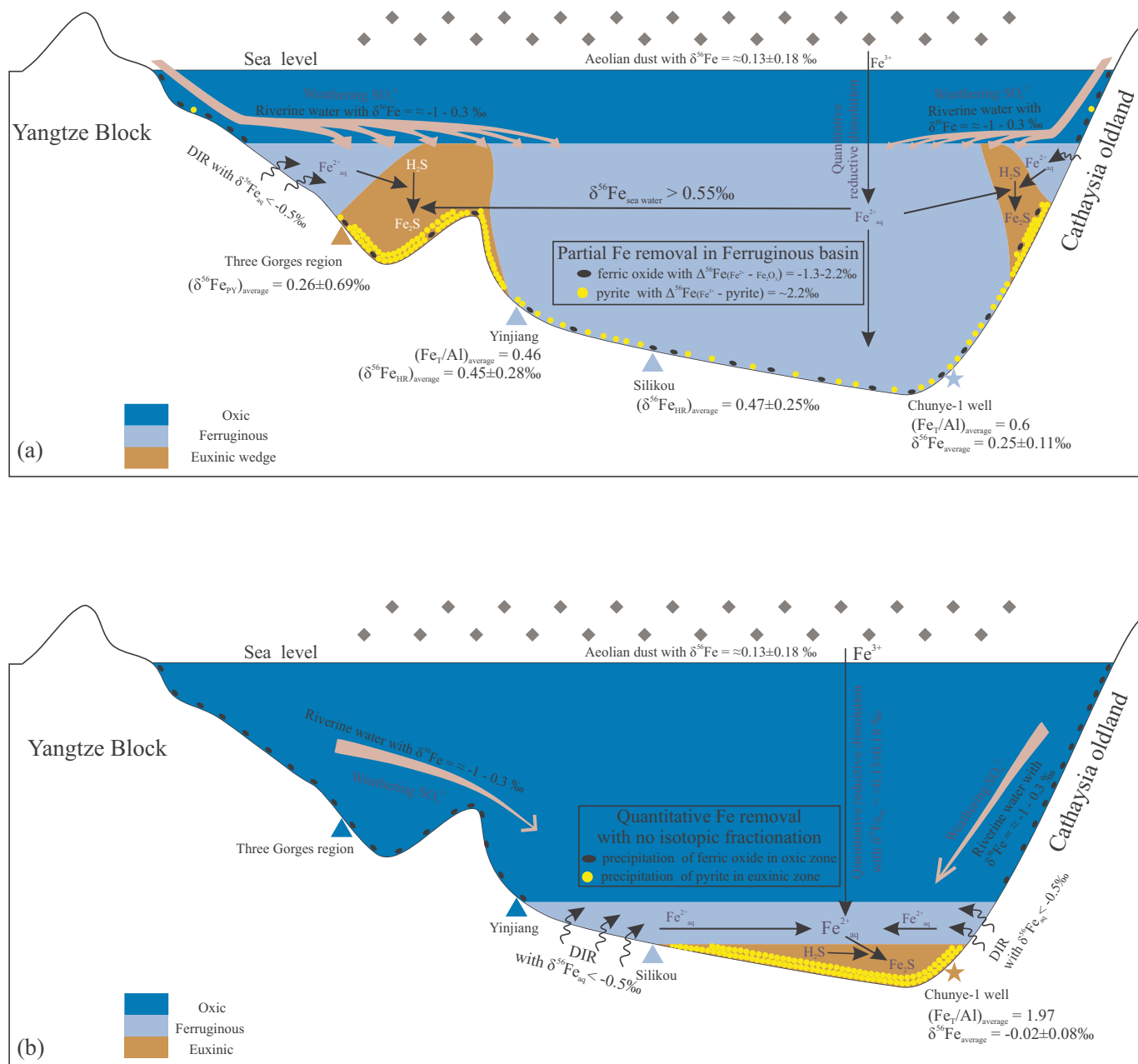


**Fig. 6.** Schematic model of the marine iron cycle during the terminal Ediacaran and Cambrian Stages 1–4 in South China. Panel A shows the scenario during the end-Ediacaran and Cambrian Stages 1–3. The values of  $\delta^{56}\text{Fe}$  in the Three Gorges region, the Yinjiang section, and the Silikou section are from Sawaki et al. (2018) and Fan et al. (2018). Panel B shows the scenario during Cambrian Stage 4. DIR—Dissimilatory iron reduction.  $\text{Fe}_{\text{aq}}^{2+}$ — $\text{Fe}^{2+}$  in aqueous phase.  $(\text{Fe}_T/\text{Al})_{\text{average}}$  and  $(\delta^{56}\text{Fe})_{\text{average}}$  represent the average values of  $\text{Fe}_T/\text{Al}$  and  $\delta^{56}\text{Fe}$ .

Formation show no evidence for deep basin  $\text{Fe}^{2+}$  oxidation throughout the terminal Ediacaran and Cambrian Stages 1–3; instead, dissolved  $\text{Fe}^{2+}$  precipitated out of solution primarily through pyritization. The low  $p\text{O}_2$  values on the Early Cambrian may have influenced the weathering behavior of redox sensitive elements exposed on land, but they were not sufficient to create an aerobic deep basin environment.

The production of biogenic sulfide in the modern oceans is rapid enough to quantitatively pyritize the incoming flux of iron several times over (Canfield, 1998). Sulfidic water masses only began to appear at mid depths, and in local basins, around the Ediacaran-Cambrian transition (Cheng et al., 2017; Feng et al., 2014; Guo et al., 2014; Li et al., 2017; Xiang et al., 2017). As the size of the oceanic  $\text{Fe}^{2+}$  reservoir during this interval was likely comparable to that of the modern ocean, this likely reflects a relatively weak flux of sulfur to marine

environments. We infer that  $p\text{O}_2$  was not only insufficient to create an aerobic deep-ocean, but was also low enough to suppress the rate of subaerial oxidative weathering of sulfides below modern levels.

Previous studies have suggested that Cambrian metazoans required oxygen levels above 10% of the present atmospheric level, but not much more than that (Sperling et al., 2015). Thus, while the shallow marine realm may have first reached the critical  $\text{O}_2$  threshold to support complex metazoans after the NOE (Wood and Erwin, 2018), the stratified redox structure of the ocean and the relatively low atmospheric  $p\text{O}_2$  ( $< 15\text{--}50\%$  PAL, Stolper and Keller, 2018) resulted in delayed oxygenation of the deep basin, lagging behind the Cambrian explosion.

Supplementary data to this article can be found online at <https://doi.org/10.1016/j.chemgeo.2020.119575>.

## Declaration of competing interest

The authors declared that they have no conflicts of interest to this work.

## Acknowledgments

We thank Weiwei Zhang and Baichan Li for their help with iron isotope analysis. We also thank anonymous reviewer and the editor Balz Kumar and Jerome Gaillardet for their very useful comments and suggestions to improve the manuscript. This work was supported by the Strategic Priority Research Program (B) of the Chinese Academy of Sciences (XDB26000000, 18000000) and the National Natural Science Foundation of China (Grant nos. 41502023, 41273081).

## References

- Anderson, T.F., Raiswell, R., 2004. Sources and mechanisms for the enrichment of highly reactive iron in euxinic Black Sea sediments. *Am. J. Sci.* 304, 203–233.
- Beard, B.L., Johnson, C.M., Skulan, J.L., Nealson, K.H., Cox, L., Sun, H., 2003. Application of Fe isotopes to tracing the geochemical and biological cycling of Fe. *Chem. Geol.* 195, 87–117.
- Bennett, S.A., Rouxel, O., Schmidt, K., Garbe-Schonberg, D., Statham, P.J., German, C.R., 2009. Iron isotope fractionation in a buoyant hydrothermal plume, 5°S Mid-Atlantic Ridge. *Geochim. Cosmochim. Acta* 73, 5619–5634.
- Bullen, T.D., White, A.F., Childs, C.W., Vivit, D.V., Schulz, M.S., 2001. Demonstration of significant abiotic iron isotope fractionation in nature. *Geology* 29, 699–702.
- Canfield, D.E., 1998. A new model for Proterozoic ocean chemistry. *Nature* 396, 450–453.
- Canfield, D.E., 2005. The early history of atmospheric oxygen: Homage to Robert A. Garrels. *Annu. Rev. Earth Planet. Sci.* 33, 1–36.
- Canfield, D.E., Teske, A., 1996. Late Proterozoic rise in atmospheric oxygen concentration inferred from phylogenetic and sulphur-isotope studies. *Nature* 382, 127–132.
- Canfield, D.E., Raiswell, R., Bottrell, S., 1992. The reactivity of sedimentary iron minerals toward sulfide. *Am. J. Sci.* 292, 659–683.
- Canfield, D.E., Poulton, S.W., Knoll, A.H., Narbonne, G.M., Ross, G., Goldberg, T., Strauss, H., 2008. Ferruginous conditions dominated later Neoproterozoic deep-water chemistry. *Science* 321, 949–952.
- Chang, H.J., Chu, X.L., Feng, L.J., Huang, J., Chen, Y.L., 2018. Marine redox stratification on the earliest Cambrian (ca. 542–529 Ma) Yangtze Platform. *Paleogeogr. Paleoclimatol. Paleocool.* 504, 75–85.
- Chen, D.Z., Wang, J.G., Qing, H.R., Yan, D.T., Li, R.W., 2009. Hydrothermal venting activities in the Early Cambrian, South China: Petrological, geochronological and stable isotopic constraints. *Chem. Geol.* 258, 168–181.
- Cheng, M., Li, C., Zhou, L., Feng, L.J., Algeo, T.J., Zhang, F.F., Romaniello, S., Jin, C.S., Ling, H.F., Jiang, S.Y., 2017. Transient deep-water oxygenation in the early Cambrian Nanhua Basin, South China. *Geochim. Cosmochim. Acta* 210, 42–58.
- Cole, D.B., Zhang, S., Planavsky, N.J., 2017. A new estimate of detrital redox-sensitive metal concentrations and variability in fluxes to marine sediments. *Geochim. Cosmochim. Acta* 215, 337–353.
- Conway, T.M., John, S.G., 2014. Quantification of dissolved iron sources to the North Atlantic Ocean. *Nature* 511, 212–215.
- Craddock, P.R., Dauphas, N., 2011. Iron isotopic compositions of geological reference materials and chondrites. *Geostand. Geoanal. Res.* 35, 101–123.
- Dauphas, N., John, S.G., Rouxel, O., 2017. Iron isotope systematics. *Rev. Mineral. Geochem.* 82, 415–510.
- Duan, Y., Severmann, S., Anbar, A.D., Lyons, T.W., Gordon, G.W., Sageman, B.B., 2010. Isotopic evidence for Fe cycling and repartitioning in ancient oxygen-deficient settings: examples from black shales of the mid-to-late Devonian Appalachian basin. *Earth Planet. Sci. Lett.* 290, 244–253.
- Eroglu, S., Schoenberg, R., Pascarelli, S., Beukes, N.J., Kleinhanns, I.C., Swanner, E.D., 2018. Open ocean vs. continentally-derived iron cycles along the Neoproterozoic Campbellrand-Malmani carbonate platform, south Africa. *Am. J. Sci.* 318, 367–408.
- Erwin, D.H., Laflamme, M., Tweedt, S.M., Sperling, E.A., Pisani, D., Peterson, K.J., 2011. The Cambrian conundrum: early divergence and later ecological success in the early history of animals. *Science* 334, 1091–1097.
- Fan, H.F., Zhu, X.K., Wen, H.J., Yan, B., Li, J., Feng, L.J., 2014. Oxygenation of Ediacaran Ocean recorded by iron isotopes. *Geochim. Cosmochim. Acta* 140, 80–94.
- Fan, H.F., Wen, H.J., Han, T., Zhu, X.K., Feng, L.J., Chang, H.J., 2018. Oceanic redox condition during the late Ediacaran (551–541 Ma), South China. *Geochim. Cosmochim. Acta* 238, 343–356.
- Feng, L.J., Li, C., Huang, J., Chang, H.J., Chu, X.L., 2014. A sulfate control on marine mid-depth euxinia on the early Cambrian (ca. 529–521 Ma) Yangtze platform, South China. *Precambrian Res.* 246, 123–133.
- Friedrich, A.J., Beard, B.L., Scherer, M.M., Johnson, C.M., 2014. Determination of the Fe (II)(aq)-magnetite equilibrium iron isotope fractionation factor using the three-isotope method and a multi-direction approach to equilibrium. *Earth Planet. Sci. Lett.* 391, 77–86.
- Guilbaud, R., Butler, I.B., Ellam, R.M., 2011. Abiotic pyrite formation produces a large Fe isotope fractionation. *Science* 332, 1548–1551.
- Guo, Q.J., Strauss, H., Zhao, Y.L., Yang, X.L., Peng, J., Yang, Y.N., Deng, Y.A., 2014. Reconstructing marine redox conditions for the transition between Cambrian Series 2 and Cambrian Series 3, Kaili area, Yangtze Platform: evidence from biogenic sulfur and degree of pyritization. *Paleogeogr. Paleoclimatol. Paleocool.* 398, 144–153.
- Halverson, G.P., Poitras, F., Hoffman, P.F., Nedelec, A., Montel, J.M., Kirby, J., 2011. Fe isotope and trace element geochemistry of the Neoproterozoic syn-glacial Rapitan iron formation. *Earth Planet. Sci. Lett.* 309, 100–112.
- Hammarlund, E.U., Gaines, R.R., Prokopenko, M.G., Qi, C.S., Hou, X.G., Canfield, D.E., 2017. Early Cambrian oxygen minimum zone-like conditions at Chengjiang. *Earth Planet. Sci. Lett.* 475, 160–168.
- Horner, T.J., Williams, H.M., Hein, J.R., Saito, M.A., Burton, K.W., Halliday, A.N., Nielsen, S.G., 2015. Persistence of deeply sourced iron in the Pacific Ocean. *Proc. Natl. Acad. Sci. U. S. A.* 112, 1292–1297.
- Huang, F., Zhang, Z.F., Lundstrom, C.C., Zhi, X.C., 2011. Iron and magnesium isotopic compositions of peridotite xenoliths from Eastern China. *Geochim. Cosmochim. Acta* 75, 3318–3334.
- Jin, C.S., Li, C., Algeo, T.J., Planavsky, N.J., Cui, H., Yang, X.L., Zhao, Y.L., Zhang, X.L., Xie, S.C., 2016. A highly redox-heterogeneous ocean in South China during the early Cambrian (similar to 529–514 Ma): Implications for biota-environment co-evolution. *Earth Planet. Sci. Lett.* 441, 38–51.
- Jin, C.S., Li, C., Algeo, T.J., Cheng, M., Lei, L.D., Zhang, Z.H., Shi, W., 2017. Evidence for marine redox control on spatial colonization of early animals during Cambrian Age 3 (c. 521–514 Ma) in South China. *Geol. Mag.* 154, 1360–1370.
- Kendall, B., Dahl, T.W., Anbar, A.D., 2017. Good Golly, why Moly? The stable isotope geochemistry of molybdenum. *Rev. Mineral. Geochem.* 82, 683–732.
- Kiczka, M., Wiederhold, J.G., Frommer, J., Voegelín, A., Kraemer, S.M., Bourdon, B., Kretzschmar, R., 2011. Iron speciation and isotope fractionation during silicate weathering and soil formation in an alpine glacier forefield chronosequence. *Geochim. Cosmochim. Acta* 75, 5559–5573.
- Klar, J.K., James, R.H., Gibbs, D., Lough, A., Parkinson, I., Milton, J.A., Hawkes, J.A., Connelly, D.P., 2017. Isotopic signature of dissolved iron delivered to the Southern Ocean from hydrothermal vents in the East Scotia Sea. *Geology* 45, 351–354.
- Kunzmann, M., Gibson, T.M., Halverson, G.P., Hodgskiss, M.S.W., Bui, T.H., Carozza, D.A., Sperling, E.A., Poirier, A., Cox, G.M., Wing, B.A., 2017. Iron isotope biogeochemistry of Neoproterozoic marine shales. *Geochim. Cosmochim. Acta* 209, 85–105.
- Li, C., Jin, C.S., Planavsky, N.J., Algeo, T.J., Cheng, M., Yang, X.L., Zhao, Y.L., Xie, S.C., 2017. Coupled oceanic oxygenation and metazoan diversification during the early-middle Cambrian? *Geology* 45, 743–746.
- Lyons, T.W., Severmann, S., 2006. A critical look at iron paleoredox proxies: New insights from modern euxinic marine basins. *Geochim. Cosmochim. Acta* 70, 5698–5722.
- Lyons, T.W., Reinhard, C.T., Planavsky, N.J., 2014. The rise of oxygen in Earth's early ocean and atmosphere. *Nature* 506, 307–315.
- Mills, B., Lenton, T.M., Watson, A.J., 2014. Proterozoic oxygen rise linked to shifting balance between seafloor and terrestrial weathering. *Proc. Natl. Acad. Sci. U. S. A.* 111, 9073–9078.
- Partin, C.A., Bekker, A., Planavsky, N.J., Scott, C.T., Gill, B.C., Li, C., Podkovyrov, V., Maslov, A., Konhauser, K.O., Lalonde, S.V., Love, G.D., Poulton, S.W., Lyons, T.W., 2013. Large-scale fluctuations in Precambrian atmospheric and oceanic oxygen levels from the record of U in shales. *Earth Planet. Sci. Lett.* 369, 284–293.
- Planavsky, N.J., McGoldrick, P., Scott, C.T., Li, C., Reinhard, C.T., Kelly, A.E., Chu, X.L., Bekker, A., Love, G.D., Lyons, T.W., 2011. Widespread iron-rich conditions in the mid-Proterozoic ocean. *Nature* 477, 448–452.
- Planavsky, N., Rouxel, O.J., Bekker, A., Hofmann, A., Little, C.T.S., Lyons, T.W., 2012. Iron isotope composition of some Archean and Proterozoic iron formations. *Geochim. Cosmochim. Acta* 80, 158–169.
- Poulton, S.W., Canfield, D.E., 2005. Development of a sequential extraction procedure for iron: implications for iron partitioning in continentally derived particulates. *Chem. Geol.* 214, 209–221.
- Poulton, S.W., Canfield, D.E., 2011. Ferruginous conditions: a dominant feature of the ocean through Earth's history. *Elements* 7, 107–112.
- Qi, C.S., Li, C., Gabbott, S.E., Ma, X.Y., Xie, L.H., Deng, W.F., Jin, C.S., Hou, X.G., 2018. Influence of redox conditions on animal distribution and soft-bodied fossil preservation of the Lower Cambrian Chengjiang Biota. *Paleogeogr. Paleoclimatol. Paleocool.* 507, 180–187.
- Radic, A., Lacan, F., Murray, J.W., 2011. Iron isotopes in the seawater of the equatorial Pacific Ocean: New constraints for the oceanic iron cycle. *Earth Planet. Sci. Lett.* 306, 1–10.
- Raiswell, R., Canfield, D.E., 2012. The iron biogeochemical cycle past and present. *Geochim. Perspect.* 1, 1–220.
- Raiswell, R., Hardisty, D.S., Lyons, T.W., Canfield, D.E., Owens, J.D., Planavsky, N.J., Poulton, S.W., Reinhard, C.T., 2018. The iron paleoredox proxies: a guide to the pitfalls, problems and proper practice. *Am. J. Sci.* 318, 491–526.
- Rolison, J.M., Stirling, C.H., Middag, R., Gault-Ringold, M., George, E., Rijkenberg, M.J.A., 2018. Iron isotope fractionation during pyrite formation in a sulfidic Precambrian ocean analogue. *Earth Planet. Sci. Lett.* 488, 1–13.
- Rouxel, O.J., Bekker, A., Edwards, K.J., 2005. Iron isotope constraints on the Archean and Paleoproterozoic ocean redox state. *Science* 307, 1088–1091.
- Sawaki, Y., Tahata, M., Komiya, T., Hirata, T., Han, J., Shu, D.G., 2018. Redox history of the Three Gorges region during the Ediacaran and Early Cambrian as indicated by the Fe isotope. *Geosci. Front.* 9, 155–172.
- Scholz, F., Schmidt, M., Hensen, C., Eroglu, S., Geilert, S., Gutjahr, M., Liebetrau, V., 2019. Shelf-to-basin iron shuttle in the Guaymas Basin, Gulf of California. *Geochim. Cosmochim. Acta* 261, 76–92.
- Severmann, S., Lyons, T.W., Anbar, A., McManus, J., Gordon, G., 2008. Modern iron isotope perspective on the benthic iron shuttle and the redox evolution of ancient oceans. *Geology* 36, 487–490.

- Sperling, E.A., Wolock, C.J., Morgan, A.S., Gill, B.C., Kunzmann, M., Halverson, G.P., Macdonald, F.A., Knoll, A.H., Johnston, D.T., 2015. Statistical analysis of iron geochemical data suggests limited late Proterozoic oxygenation. *Nature* 523, 451–454.
- Stolper, D.A., Keller, C.B., 2018. A record of deep-ocean dissolved O<sub>2</sub> from the oxidation state of iron in submarine basalts. *Nature* 553, 323–327.
- Waeles, M., Baker, A.R., Jickells, T., Hoogewerff, J., 2007. Global dust teleconnections: aerosol iron solubility and stable isotope composition. *Environ. Chem.* 4, 233–237.
- Welch, S.A., Beard, B.L., Johnson, C.M., Braterman, P.S., 2003. Kinetic and equilibrium Fe isotope fractionation between aqueous Fe(II) and Fe(III). *Geochim. Cosmochim. Acta* 67, 4231–4250.
- Wen, H.J., Fan, H.F., Zhang, Y.X., Cloquet, C., Carignan, J., 2015. Reconstruction of early Cambrian ocean chemistry from Mo isotopes. *Geochim. Cosmochim. Acta* 164, 1–16.
- Wiesli, R.A., Beard, B.L., Johnson, C.M., 2004. Experimental determination of Fe isotope fractionation between aqueous Fe(II), siderite and “green rust” in abiotic systems. *Chem. Geol.* 211, 343–362.
- Wood, R., Erwin, D.H., 2018. Innovation not recovery: dynamic redox promotes metazoan radiations. *Biol. Rev.* 93, 863–873.
- Xia, Y., Li, S.Q., Huang, F., 2017. Iron and Zinc isotope fractionation during magmatism in the continental crust: evidence from bimodal volcanic rocks from Hailar basin, NE China. *Geochim. Cosmochim. Acta* 213, 35–46.
- Xiang, L., Schoepfer, S.D., Shen, S.Z., Cao, C.Q., Zhang, H., 2017. Evolution of oceanic molybdenum and uranium reservoir size around the Ediacaran-Cambrian transition: evidence from western Zhejiang, South China. *Earth Planet. Sci. Lett.* 464, 84–94.
- Yuan, Y.Y., Cai, C.F., Wang, T.K., Xiang, L., Jia, L.Q., Chen, Y., 2014. Redox condition during Ediacaran-Cambrian transition in the Lower Yangtze deep water basin, South China: Constraints from iron speciation and  $\delta^{13}\text{C}_{\text{org}}$  in the Diben section, Zhejiang. *Chin. Sci. Bull.* 59, 3638–3649.
- Zhang, F.F., Zhu, X.K., Yan, B., Kendall, B., Peng, X., Li, J., Algeo, T.J., Romaniello, S., 2015. Oxygenation of a Cryogenian ocean (Nanhua Basin, South China) revealed by pyrite Fe isotope compositions. *Earth Planet. Sci. Lett.* 429, 11–19.
- Zhu, M.Y., Zhuravlev, A.Y., Wood, R.A., Zhao, F.C., Sukhov, S.S., 2017. A deep root for the Cambrian explosion: implications of new bio-and chemostratigraphy from the Siberian Platform. *Geology* 45, 459–462.